Biosensors and Bioelectronics 131 (2019) 224–231

Contents lists available at ScienceDirect

Biosensors and Bioelectronics

journal homepage: www.elsevier.com/locate/bios

A "time-frozen" technique in microchannel used for the thermodynamic studies of DNA origami

Peng Huang[a,b,1], Jingwen Wang[a,1], Long Jiao[c], Dandan Gu[a], Shusen Jiang[a], Mingpo Li[a], Wenlong lv[a], Hong Chen[a,*], Hao Pei[d,*]

[a] Pen-Tung Sah Institute of Micro-Nano Science and Technology, Xiamen University, Xiamen 361005, PR China
[b] College of Chemisty and Chemical Engineering, Xiamen University, Xiamen 361005, PR China
[c] College of Chemistry and Chemical Engineering, Xi'an Shiyou University, Xi'an 710065, PR China
[d] Shanghai Key Laboratory of Green Chemistry and Chemical Processes, School of Chemistry and Molecular Engineering, East China Normal University, Shanghai 200241, PR China

ARTICLE INFO

Keywords:
DNA nanotechnology
Origami
Microchannel
Thermodynamics

ABSTRACT

The emergence of DNA origami greatly accelerated the development of DNA nanotechnology. A thorough understanding of origami thermodynamics is very important for both fundamental studies and practical applications. These thermodynamic transitions usually take place in several seconds or even less, and are very difficult to monitor by conventional methods. Numerous tests are required to characterize the origami molecule's behaviors at different temperatures, which is very labor-intensive and time-consuming. In this paper, an axially distributed temperature gradient along a capillary was formed in a spatially varying temperature field. In such a temperature gradient, the origami molecule's thermodynamic processes occur and remain stable at every position along the capillary's microchannel. It looks like the time of the thermodynamic process is frozen along the microchannel. With this method, the origami molecule's thermodynamic characteristics at different temperatures can be obtained in a single experiment, and rapid processes can be monitored with ease by conventional methods for an adequate time period at low cost. In order to show its potential abilities, this method has been demonstrated in applications which the origami's assembly, denaturation and strand displacement are carry out in a flowing or stationary solution.

1. Introduction

In 2006, Rothemund reported the DNA origami method, which promotes the rapid development of structures for DNA nanotechnology (Rothemund, 2006; Torring et al., 2011; Seeman, 2007). This method allows the formation of arbitrary 2D or 3D nanostructures (Liu et al., 2011; Douglas et al., 2009a; Andersen et al., 2009; Han et al., 2011; Dietz et al., 2009). During the assembly process, M13 and pre-designed staple strands are first mixed, and the assembly occurs in the subsequent annealing step (Castro et al., 2011; Douglas et al., 2009b). DNA origami possesses many unique characteristics useful for applications in different areas, *e.g.*, precise positioning of nanoparticles or molecules (Derr et al., 2012; Ding et al., 2010; Fu et al., 2013), surface enhanced Raman spectroscopy (Kühler et al., 2014), and drug delivery (Jiang et al., 2012). Currently, DNA origami is receiving widespread attention and been used in numerous areas (Sacca and Niemeyer, 2012; Pinheiro et al., 2011; Nangreave et al., 2010).

DNA origami is very sensitive to temperature, which can affect its state and properties. Many dynamic responses of origami are produced by temperature changes. These dynamic processes generally correspond to the characteristics and functions of origami and therefore have meaning and value for research. Thermodynamic and kinetic studies of DNA nanostructures is useful for identifying optimal structural characteristics, efficient assembly procedures, precise positioning and modification of functional groups, and developing many interesting applications (Wei et al., 2014; Qu et al., 2017a, 2017b; Lai et al., 2018; Yao et al., 2015). Much research work has been reported to investigate the origami's thermodynamic characteristics. Using thermally controlled atomic force microscopy (AFM), Song *et al.* investigated the melting process of origami and revealed the reversible association/

* Corresponding authors.
E-mail addresses: hongc@xmu.edu.cn (H. Chen), peihao@chem.ecnu.edu.cn (H. Pei).
[1] P. Huang and J. Wang have equal contribution to this work. P. Huang is currently working at ShenZhen HaploX Biotechnology Co., LTD, Shenzhen 518000, P. R. China.

https://doi.org/10.1016/j.bios.2019.02.012
Received 30 November 2018; Received in revised form 1 February 2019; Accepted 10 February 2019
Available online 19 February 2019
0956-5663/

dissociation process of origami (Song et al., 2012). They also studied the isothermal hybridization kinetics of multistrand DNA on DNA origami nanopores (Song et al., 2013). Wei *et al.* used fluorescence resonance energy transfer (FRET) to monitor the assembly and melting of origami and examined the effects of local and long-range structural defects on the thermal stability of common origami structures (Wei et al., 2013). To avoid misfolded structures in the origami assembly, Dunn *et al.* investigated the folding pathways and thermodynamics of DNA origami (Dunn et al., 2015). Wah et al. investigated the assembly and dissociation of DNA origami and found that significant structural changes were observed between 65 °C and 55 °C (Wah et al., 2016). In most of these studies, the origami molecule's state or property under different temperatures needed to be collected or characterized one by one, which is labor-intensive and time-consuming. These dynamic processes usually take place in several seconds or even less. The performance of current instruments and methods is insufficient to obtain and analyze the signals from rapid dynamic processes. Only the origami molecule's stable state can be investigated unless expensive or special instrumentation is used.

Microfluidic chips can be applied to study origami thermodynamics and kinetics, thereby overcoming the disadvantages of conventional approaches. Microfluidic chips achieve specific functions and applications through automated manipulation of an extremely low volume of fluids in microchannels and microstructures (Whitesides, 2006) and possess advantages, such as rapid diffusion, small sample volume, short time, high throughput, convenient operation, and high integration of processes. In addition, because of the miniaturization, portability, and automation of the instrumentation, this technique has been widely used for biomedical detection (Shi et al., 2008; Clausell-Tormos et al., 2008; Cai et al., 2012), immunoassays (Sato et al., 2003), diagnosis (Yager et al., 2006), and other applications. Microfluidic chips can transform temporal dynamic changes to spatial distributions (Garcia et al., 2007); *i.e.,* the dynamic process change can be set up as a stable distribution along the microchannel. As a result, it can achieve and fix the origami molecule's thermodynamic states under a spatial distribution as a temperature gradient along the microchannel. This technique will provide sufficient time to investigate rapid dynamic processes, and obtain all the characteristics of different temperatures in a single test. However, the current microfluidic chips have shortcomings, such as a complex structure, difficult processing, and high cost (Lee et al., 2005; Chiu et al., 2009; Kakuta et al., 2003). Several studies have reported using capillaries to replace microfluidic chips for applications, including enzyme inhibition assays, single cell analysis, high-throughput drug screening and so on (Du et al., 2006; Gu et al., 2011; Jin et al., 2014). The capillary-based analysis methods not only possess the characteristics of microfluidic chips but also possess other advantages, such as easy operation and low cost. In our previous works, DNA, aptamer and nucleotide had been used for the detection of microRNA, metal ion and Glucose (Qi et al., 2017a, 2017b; Chen et al., 2017; Zhong et al., 2018). The DNA and aptamer arrays were also generated along the capillary and served as a sensitive analytical platform for a variety of molecules, including DNA, protein, drug and metal ions (Qu et al., 2012, 2017c, 2017d, 2017e).

This paper proposes a capillary-based technique to facilitate and accelerate the study of origami thermodynamics. An axially distributed temperature gradient is formed along the capillary in a spatially varying temperature field, which transforms the temporal gradient of temperature to a spatial temperature gradient along the capillary's microchannel. The dynamic process caused by the temperature change can be set up as a stable distribution of this process along the microchannel. The sequential states of the thermodynamic process appear at the continuous positions along the capillary and keeps stable, it looks like that the time of the dynamic process was frozen, which was called “time-frozen” technique here. As a result, this “time-frozen” technique achieves and fixes the process under all the temperatures in a single experiment, which also provides sufficient convenience such that routine instruments and methods can be used to investigate the thermodynamics and kinetics of their rapid responses. To show this method's capability, several thermodynamic processes (including dynamic assembly, strands displacement and localized investigation of origami assembly and denaturation) are demonstrated in this paper.

2. Materials and methods

2.1. Chemicals and reagents

M13mp18 was purchased from New England Biolabs (Beijing, China). The staple strands were purchased from Life Technologies Ltd. (Shanghai, China) and purified using PAGE. The staple strands (identified as 1–1 and 19–1), which were labeled with 6-FAM and Dabcyl, respectively, were purchased from Sangon Biotech Co., Ltd. (Shanghai, China) and purified using ULTRAPAGE. The sequence information of all staple strands can be found in the Supporting Information. The other reagents were all analytical grades and purchased from Sinopharm Chemical Reagent Co., Ltd. (Beijing, China) and Aladdin (Shanghai, China).

2.2. Establishment of a temperature gradient and online detection system

The setup shown in Fig. 1A was used to establish the temperature gradient which can be used to fix the origami's thermodynamic process along the microchannel. Hot air form a hot air gun (Atten Technology Co., Ltd, Shenzhen, China) was used to create a spatially temperature field around the outlet of the hot air gun. The air speed and the temperature were controlled to vary the temperature field. A capillary (diameter of 1 mm) was inside the temperature field and vertical with respect to the hot air gun, and the left end of capillary was connected to a syringe. A precision syringe pump (LSP02-1B, Longer Pump Co., Ltd, Baoding, China) with the volume flow from 0.831 nl/min to 150.5 ml/min was used to drive the solution in the syringe to flow through the capillary. The outflow liquid was collected from the right end of the capillary. After the spatially varying temperature field stabilized, an axially distributed temperature gradient along the capillary was then established. A thermo couple probe (OMEGA Engineering, INC., Norwalk, USA) with an ultrafine tip (diameter of 0.35 mm) was inserted into the capillary to measure the temperature at the different positions of the capillary.

FRET was used to monitor the variation in the fluorescence intensity during the thermodynamic process, thus providing real-time information of the process. A laser with a wavelength of 488 nm (MLL-III-488L, Changchun New Industries Optoelectronics Tech. Co., Ltd., Changchun, China) was installed on the right end of the capillary. The laser was adjusted to axially penetrate the whole capillary to excite the fluorescent functional groups in the solution. A cooled charge coupled device (CCD) (Alta U4000, Apogee Imaging Systems, USA) was installed on the side of capillary, and the excited fluorescence was collected by the CCD through a bandpass filter.

2.3. Origami's thermodynamic processes in flowing or stationary state

As a prototype application, DNA origami was dynamic assembled during the flowing by this method. M13 and staple strands were mixed in a 1:5 ratio in 1 × TAE-Mg^{2+} buffer solution (40 mM Tris, 2 mM EDTA and 12.5 mM $MgCl_2$), in which the final M13 concentration was 10 nM. After the temperature gradient along the capillary was established, the mixture solution was driven by the syringe pump to flow through the capillary, and the outflow liquid containing the assembled origami was collected. FRET and AFM was used to realize the online and offline detection the assembly.

The thermodynamic applications which the solution inside the microchannel was kept in the stationary state were also demonstrated. The capillary's microchannel was filled with the origami or pre-mixed

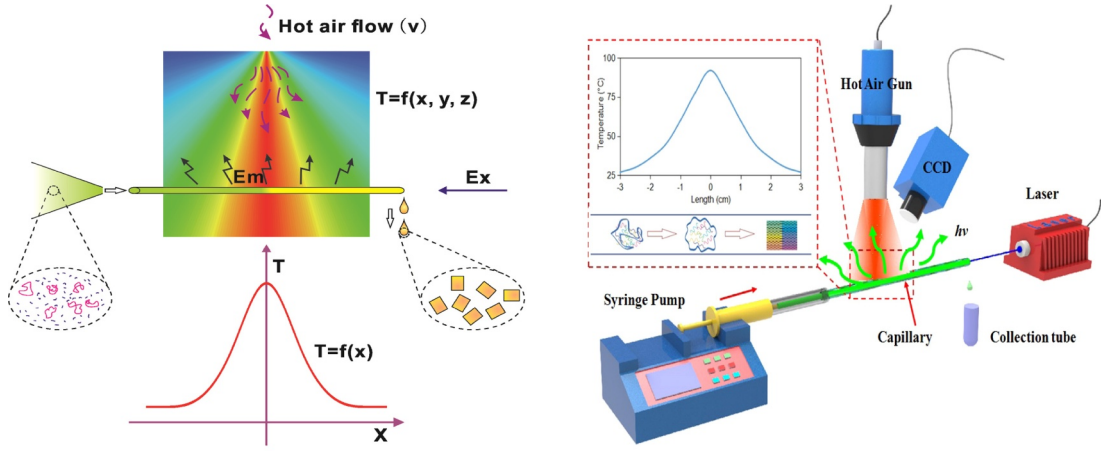

(A)

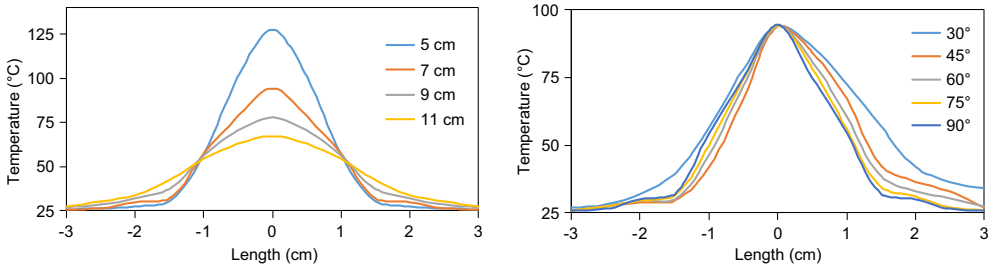

(B)

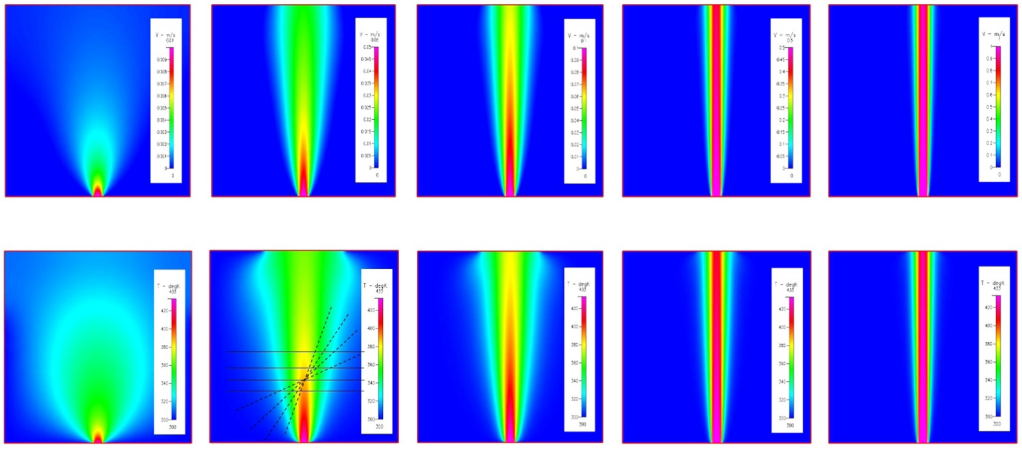

(C)

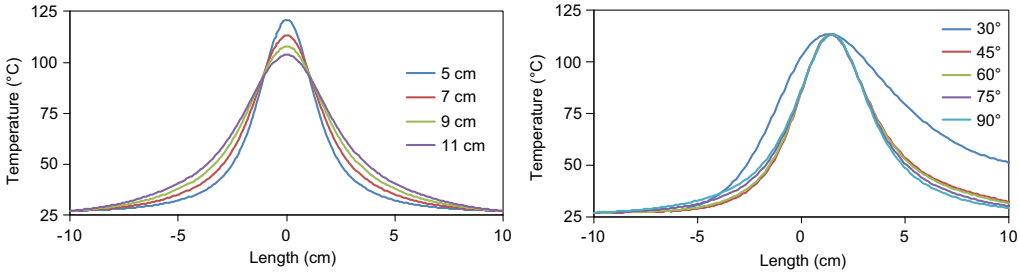

(D)

(caption on next page)

Fig. 1. (A) Schematic diagram of the setup used for the establishment of the temperature gradient and fluorescence detection; (B) Left: the measured temperature distribution curves when the capillary was perpendicular to and 5 cm, 7 cm, 9 cm, and 11 cm away from the hot air gun, right: the measured temperature distribution curves when the angle between the capillary and the hot air gun was 90°, 75°, 60°, 45°, and 30°; (C) Upper: the simulated flow fields when the air speed was 1 cm/s, 5 cm/s, 10 cm/s, 50 cm/s and 100 cm/s, lower: the simulated temperature fields when the air speed was 1 cm/s, 5 cm/s, 10 cm/s, 50 cm/s and 100 cm/s; (D) Left: the simulated temperature distribution curves when the capillary was perpendicular to and 5 cm, 7 cm, 9 cm, and 11 cm away from the hot air gun, right: the simulated temperature distribution curves when the angle between the capillary and the hot air gun was 90°, 75°, 60°, 45°, and 30°.

solution and then kept statically. The temperature gradient along the capillary was then established to initiate the thermodynamic process. AFM and FRET were used to perform the offline and online monitoring of the process.

2.4. Offline detection of origami

AFM (Multimode Nanoscope IIIa, Vecco/Digital Instruments, USA) was used for offline characterization of the origami in the collected solution. The basic process was as follows: 2 μl of the collected solution was dropped on a freshly cleaved mica surface for adsorption for 5 min; 10 μl of buffer solution was added to stop the adsorption process; and tapping mode AFM in liquid was used to scan the mica surface.

3. Results and discussion

3.1. Temperature gradient and "time-frozen" technique

Origami is very sensitive to temperature or its change, so its thermodynamic study is very important in its relative processes. In most reports, the thermodynamic process was studied under the varying temperatures over time, and the temperature variation can be described as $grad(T) = \frac{dT}{d\tau}$ (where T is temperature, and τ is time). In this paper, the temporal temperature gradient was replaced with a spatial temperature gradient; the expression of the temperature field is $grad(T) = \frac{\partial T}{\partial x}i + \frac{\partial T}{\partial y}j + \frac{\partial T}{\partial z}k$ (where i, j, and k denote the unit vectors for x, y, and z, respectively). A capillary was placed at a particular position inside the spatially varying temperature field such that a gradually increasing and then gradually decreasing temperature gradient was formed axially along the capillary. The expression of the temperature gradient can be simplified as $grad(T) = \frac{dT}{dx}i$ or $grad(T) = \frac{dT}{dr}r$ (r is the unit vector along the axial direction of the capillary).

In this paper, the hot air blown out of the hot air gun was used to create a symmetrical temperature gradient distributed along the axial direction of the capillary (as shown in Fig. 1A). A thermocouple was used to measure the temperature at each position inside the empty capillary. When the capillary was perpendicular to and 5 cm, 7 cm, 9 cm, and 11 cm away from the hot air gun, the maximum temperature at the center was 127 °C, 94 °C, 78 °C, and 67 °C, respectively, as shown in the temperature distribution (Fig. 1B curve left panel). When the capillary was closer to the hot air gun, the temperature at the center of the capillary was higher. Additionally, the distribution region of the temperature gradient was relatively narrow, *i.e.*, the temperature distribution curve was steeper when the capillary was closer. As the distance from the hot air gun increased, the temperature at the center gradually decreased; the temperature gradient also gradually expanded to the two sides, forming a smoother temperature distribution curve. To obtain a denaturation temperature that was as high as possible and also prevent the solution in the capillary from boiling, the capillary was placed 7 cm away from the hot air gun. When the capillary formed certain angles with the outlet of the hot air gun, an unsymmetrical temperature gradient was formed along the capillary. The temperature distribution curves for when the angle was 90°, 75°, 60°, 45°, and 30° are shown in the right panel of Fig. 1B. Compared to the perpendicular position, for positions with decreases in the angle, the temperature gradient to the left of the maximum temperature gradually decreased while that to the right gradually extended. When the angle was 30°, the temperature gradient on both sides of the maximum temperature exhibited some extension, albeit higher on the right side.

The flow field and temperature field caused by the hot air gun was further computationally simulated. The flow field and temperature field (shown as the upper and lower rows, respectively, in Fig. 1C) formed in the 20 cm × 20 cm 2D space, where the hot air was blown out from the center of the bottom (1 cm in length). The initial temperature of the hot air was set to be 160 °C, and the air speed was 1 cm/s, 5 cm/s, 10 cm/s, 50 cm/s, and 100 cm/s, respectively. For the air speed of 1 cm/s, which is very low, the flow field and temperature field were different from those caused by the other air speeds. At the other air speeds, the range of the high temperature region at the center gradually increased with increasing air speed; however, the temperature gradient was also much steeper. At low air speeds, the high temperature region at the center was very small. However, the relatively low speed provided more time for heat diffusion, thus forming a flatter and wider temperature gradient. The temperature gradients that formed when the air speed was 5 cm/s and the capillary was 5 cm, 7 cm, 9 cm, and 11 cm away from and perpendicular to the outlet of the hot air gun are shown in the left panel of Fig. 1D (*i.e.*, the temperature gradient along the solid line in the second figure of the second row in Fig. 1C). With increases in the distance, the maximum temperature at the center gradually deceased and the temperature gradient also expanded to both sides. The result from the simulation shows the effect of varying conditions and reveal the variation trend, which is agree with the result form the measurement.

The temperature distribution obtained from simulations when the distance between the capillary and the hot air gun was 7 cm, the air speed was 5 cm/s, and the angle between the two was 30°, 45°, 60°, 75° and 90° is shown in the right panel of Fig. 1D (*i.e.*, the temperature gradient along the dashed line in the second figure of the second row in Fig. 1C). The different temperature gradients on the two sides of the maximum temperature exhibited a similar trend and variation compared with that of the experimental measurements.

The temperature gradient along the capillary was generated through the heat transfer process, so it can be described as: $T = \frac{k}{\sqrt{\tau}}e^{-\frac{x^2}{4D\tau}}$, where T and x are the temperature and position along the capillary, k and D are coefficients, τ is the time to form the temperature gradient by heat transfer. The time τ is determined by the hot air velocity (v) and the distance of the capillary to the hot air gun (s): $\tau = s/v$. The position with a certain temperature along the capillary can be calculated by: $x = \sqrt{-4D\frac{s}{v}\ln(\frac{T}{k}\sqrt{\frac{s}{v}})}$ or $T = k\sqrt{\frac{v}{s}}e^{-\frac{vx^2}{4Ds}}$. The corresponding positions to the temperatures which the origami's thermodynamic transitions occur at or between can be calculated accurately by this equation, and vice verse. The spatial resolution of the temperature along the capillary is: $\frac{dT}{dx} = -\frac{kvx}{2Ds}\sqrt{\frac{v}{s}}e^{-\frac{vx^2}{4Ds}}$. During the annealing of the conventional method, the temperature usually decreases with the time: $T = a - bt$, where a and b are the initial temperature and the cooling rate, T and t are the temperature and time. The corresponding position on the capillary whose temperature equals to that at a certain time during the conventional annealing is: $x = \sqrt{-4D\frac{s}{v}\ln(\frac{(a-bt)}{k}\sqrt{\frac{s}{v}})}$ or $t = (a - k\sqrt{\frac{v}{s}}e^{-\frac{vx^2}{4Ds}})/b$. The temporal gradient of temperature in the conventional method is then transformed to the spatial temperature distribution along the capillary, and vice verse. The spatial resolution of the time (elapsed in the conventional method) is: $\frac{dt}{dx} = \frac{kvx}{2Dbs}\sqrt{\frac{v}{s}}e^{-\frac{vx^2}{4Ds}}$. By adjusting the parameters, the different spatial resolutions of temperature and time can be realized along the capillary to facilitate the study

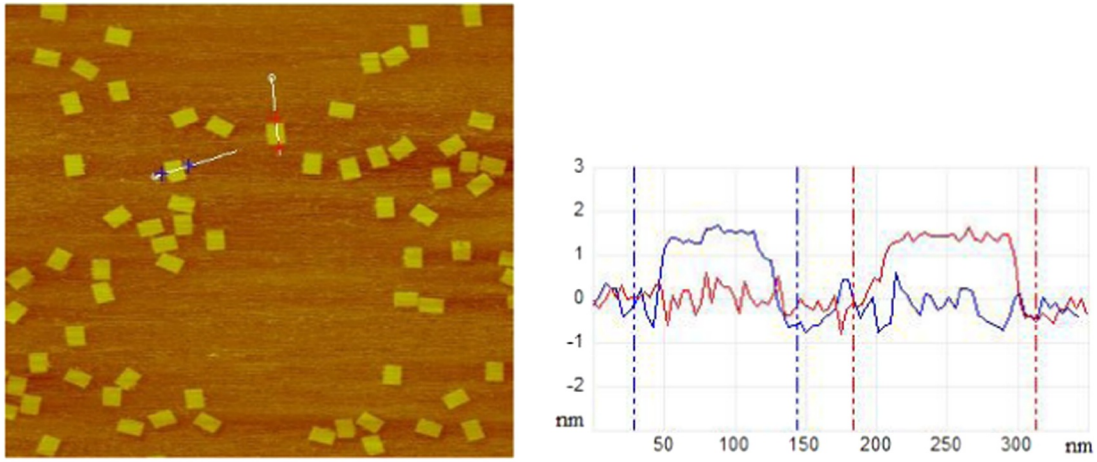

(A)

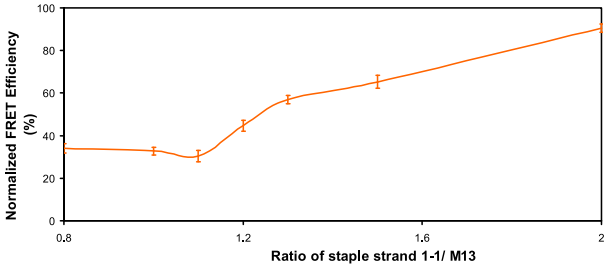

(B)

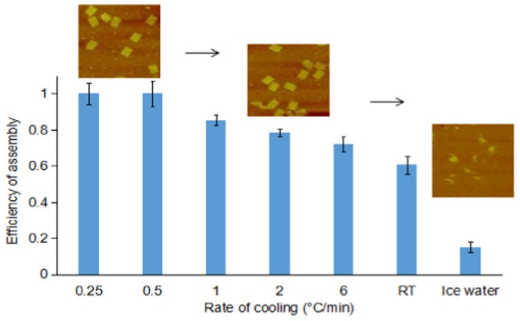

(C)

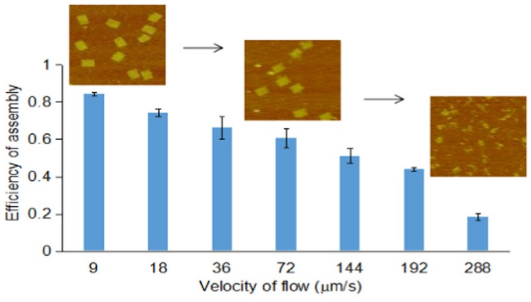

(D)

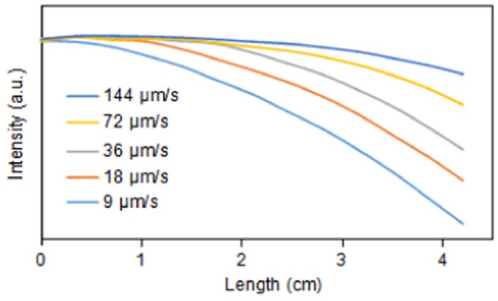

(E)

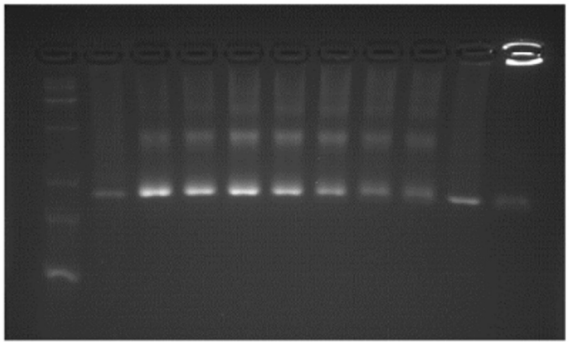

(F)

Fig. 2. (A) AFM image of the origami and its height profile; (B) The normalized FRET efficiency compared to before assembly with different staple strand 1–1/M13 ratios; (C) The assembly efficiency calculated according to FRET and AFM images for the different cooling rates in the conventional method; (D) The assembly efficiency calculated according to FRET and AFM images for the different flow rates in the dynamic assembly; (E) The fluorescence intensity for the dynamic assembly under different flow rates along the microchannel, the position 0 is the center of the temperature gradient which is 94 °C; (F) The gel electrophoresis image of the origami assembled under different conditions (lane 1: DNA ladder; lane 2: assembled by the conventional method; lane 3–9: assembled by the dynamic assembly, and the flow rates are 9 μm/s, 18 μm/s, 36 μm/s, 72 μm/s, 144 μm/s, 192 μm/s and 288 μm/s; lane 10: the denaturation behavior of the assembled origami in the temperature gradient; lane 11: the assembly behavior of the pre-mixed solution in the temperature gradient.

on the origami's certain thermodynamic transition.

3.2. Dynamic assembly of DNA origami during flowing

The origami's dynamic assembly was developed to show the proposed technique's capability in the flowing system. In most reports, origami is assembled through the stationary annealing method, *i.e.*, a pre-mixed solution is in a stationary state. In this paper, the temporal temperature gradient for the conventional annealing method was replaced with a spatial temperature gradient. The annealing of the pre-mixed solution was completed after the solution flowed through the temperature gradient, thus providing the dynamic assembly of origami.

Rectangular origami was used in the paper (as shown in Fig. 2A), and the design schematic is shown in the Supporting Information; the size was 90 nm × 70 nm. In addition to the AFM characterization of the morphology of the assembled origami, FRET was used to monitor the assembly process and assembly efficiency. Two adjacent staple strands (the 5′ end of strand number 1–1 and the 3′ end of strand number 19–1) were labeled with the fluorescent dye 6-FAM and the fluorescent quencher Dabcyl, respectively. Before the origami assembly, the two staple strands were free in solution, and the fluorescent group could emit strong fluorescence after excitation. However, after assembly, the fluorescent group and the quencher group were brought into close proximity; thus, the fluorescence intensity decreased considerably because of FRET. The FRET efficiency (E), which is related to the change in distance between the FRET donor and acceptor, is defined by the following equation: $E = 1 - F_{DA}/F_D$, where F_D and F_{DA} are the fluorescent intensity of the donor in the absence or presence of the acceptor, respectively (Wei et al., 2013). In this study, the measured FRET efficiency between the 6-FAM and the Dabcyl group was 70.0 ± 2.7%.

To determine the assembly efficiency, a fluorescence spectrophotometer (F-7000, Hitachi, Ltd., Japan) and cooled CCD were used for offline and online measurements of the fluorescence intensity due to FRET. First, fluorescence background needed to be reduced to improve the detection sensitivity and to more accurately calculate the efficiency of origami assembly. Therefore, the amount of staple strand number 1–1 should be minimized to the smallest amount sufficient for the assembly. The ratio of M13 to the other staple strands was maintained at 1:5; the ratio of M13 to staple strand number 1–1 staple strand was adjusted to 1:0.8, 1:1, 1:1.1, 1:1.2, 1:1.3, 1:1.5, and 1:2. The conventional method was used for the origami assembly, and the fluorescence spectrophotometer was used to measure the fluorescence intensity before and after the assembly; the results are shown in Fig. 2B. The normalized FRET efficiency (F_A/F_B, expressed as a percentage) decreased after assembly (F_A) compared to before assembly (F_B), indicating that when there was a sufficient amount of staple strand number 1–1, this strand participated in the assembly. When the ratio was increased from 1:0.8–1:1.1, the normalized FRET efficiency was approximately 30.4%; as the ratio further increased, the normalized FRET efficiency gradually increased to 90.5%. Theoretically, when the ratio was 1:1, all of staple strand number 1–1 should pair with M13; there should be no unpaired staple strand number 1–1 and M13 after assembly, and the fluorescence intensity should decrease to the minimum. However, in real situation, there is an operational error in transferring small amounts of solution. As a result, to ensure that all M13 are paired with staple strand number 1–1, a ratio of 1:1.1 was chosen for the subsequent assembly. Assume that the origami assembly efficiency is 100% at this ratio (*i.e.*, all M13 has been assembled to form origami). The assembly efficiency in the later part of the paper will be calculated by referring to this relative ratio.

In the conventional assembly process, the annealing normally takes approximately 2 h; there was also literature report showing that the origami assembly can be achieved with tens of minutes of annealing (Fu et al., 2013). To study the required flow rate for the dynamic assembly, the conventional method was used to investigate the effects of different cooling rates on the assembly. The cooling rate in the temperature cycle controller was set to 0.25 °C/min, 0.5 °C/min, 1 °C/min, 2 °C/min and 6 °C/min (cooled from 95 °C to 25 °C). In addition, the denatured solution was also placed directly in room temperature (rapid cooling; reaching room temperature after 1 min, *i.e.*, a cooling rate of 70 °C/min) and ice water (extremely rapid cooling, reaching 0 °C in 15 s, *i.e.*, a cooling rate of 380 °C/min) to investigate the limit of the cooling rates required for the assembly. The assembly efficiency calculated according to FRET and AFM images for the different cooling rates are shown in Fig. 2C. The AFM results show that rectangular origami can be assembled for the various cooling rates except for the extremely rapid cooling rate. However, the FRET results show that when the cooling rate was increased from 0.5 °C/min to 70 °C/min, the assembly efficiency gradually decreased from approximately 100–60.6%. When the cooling rate was further increased to 380 °C/min, the assembly efficiency decreased to 15.2%. For these rapid cooling conditions (as short as 1 min of annealing time), the AFM results showed excellent origami morphology; however, the FRET results indicated that perfect assembly may not have occurred for the fine structures. Therefore, to obtain perfect assembled origami through the conventional method, at least 2 h of annealing time is recommended; if only a limited quality of origami structures is required, rapid cooling can be used.

The annealing process can be achieved from the flow of the pre-mixed solution along the temperature gradient, and the cooling rate is determined by the flow rate of solution in the capillary. The effect of different flow rates (9 μm/s, 18 μm/s, 36 μm/s, 72 μm/s, 144 μm/s, 192 μm/s, and 288 μm/s with corresponding average cooling rates of 1.5 °C/min, 3 °C/min, 6 °C/min, 12 °C/min, 24 °C/min, 32 °C/min, and 48 °C/min, respectively) on the dynamic assembly was investigated. The resulting assembly efficiency and AFM images are shown in Fig. 2D, respectively. When the flow rate was less than 72 μm/s, intact rectangular origami can be obtained, as shown in AFM results. As the flow rate increased further, origami with a partially intact structure gradually appeared. When the flow rate was greater than 288 μm/s, no intact origami was observed by AFM. The variation in the assembly efficiency also exhibited this trend; the assembly efficiency gradually decreased from 84.5% to 18.4% with increasing flow rate. The fluorescence intensity for the dynamic assembly under different flow rates along the axial direction of the capillary is shown in Fig. 2E. The curves began from the center of the temperature gradient which had highest fluorescence intensity. The fluorescence gradually decreased from left to right, indicating that the pre-mixed solution assembled during the flow process. The decrease in the fluorescence intensity was more pronounced for low flow rates, indicating that the assembly efficiency of origami was higher when the flow rate was low. In contrast, the assembly efficiency gradually decreased with increasing flow rate. The outflow solutions generated at different flow rates were collected and separated by gel electrophoresis. A distinct origami band appeared in the gel electrophoresis image for all solutions. The intensity of the band decreased and the boundary of the band also gradually became blurred with increasing flow rate (as shown in lane 3 - lane 9 in Fig. 2F). With this dynamic assembly method, the origami can be assembled continuously with more output in less time, and the whole process can be online monitored to ensure better quality in a low-cost way.

3.3. DNA origami's thermodynamics in stationary state

The “time-frozen” technique can be also used in those thermodynamic studies which the solution is kept stationary inside the microchannel. It has the ability of investigating the thermodynamic process under all the temperatures simultaneously, which provides sufficient time such that routine instruments and methods can be used to characterize the thermodynamics and kinetics of these rapid responses. Some thermodynamic processes have been chosen in this paper as examples to show its capability.

The effect of different temperatures on strand displacement reactions was investigated inside the capillary. The staple strand number

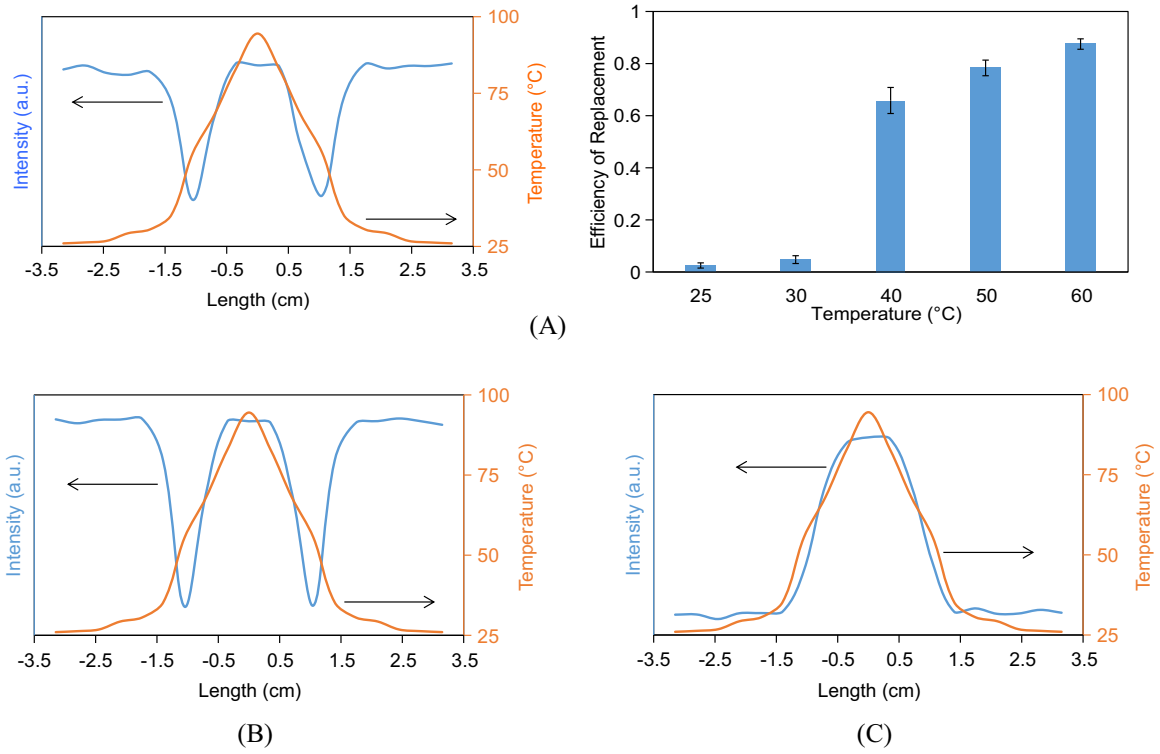

Fig. 3. (A) Left: the fluorescence and temperature distribution curves along the temperature gradient during the strand displacement reaction, right: the efficiencies of the strand displacement reactions in bulk solution under different temperatures; (B) The fluorescence and temperature distribution curves along the temperature gradient to monitor the assembly behavior of the pre-mixed solution at different temperatures; (C) The fluorescence and temperature distribution curves along the temperature gradient to monitor the denaturation behavior of the assembled origami at different temperatures.

19–1 contains 40 bases and was labeled with the quenching group Dabcyl at its 3′ end. The 19–2 staple strand was synthesized, which lacks 16 bases and the Dabcyl labeling that are found in staple strand number 19–1. The 19–2 staple strand was used instead of staple strand number 19–1 in the origami assembly performed using the conventional method. Then, the 19–1 staple strand was mixed with the assembled origami at a ratio of 1:1; the strand displacement reaction was then carried out under the effect of the temperature gradient in the capillary. The results are shown in the left panel of Fig. 3A. Because the temperature on the two sides of the capillary was low, the rate of the strand displacement reaction was very low. As a result, the fluorescence groups in origami were not quenched and therefore emitted strong fluorescence when excited. The temperature gradually increased when the temperature gradient moved to the center of the capillary; thus, the rate of the strand displacement reaction also gradually increased. As the amount of the 19–2 staple strand displaced by staple strand number 19–1 increased, more and more fluorescent groups were quenched by the quenching groups in staple strand number 19–1, resulting in a gradual decrease in the fluorescence that was excited in the solution. When the temperature was further increased to exceed the denaturation temperature of origami, all number 1–1 staple strands labeled with 6-FAM dissociated into the solution and could be excited to give a high fluorescence intensity. The strand displacement reaction was also performed in the bulk solution to compare with that performed inside the capillary; the results are shown in the right panel of Fig. 3A. When the reaction temperature was lower than 30 °C, the rate of the strand displacement reaction was very low; when the temperature increased from 40 °C to 60 °C, the rate of the strand displacement reaction gradually increased from 65.8% to 87.5%. When the temperature was further increased, the temperature could exceed the denaturation temperature, resulting in dissociation of origami. Compared with that in the bulk solution, the replacement reaction rates under all the temperatures can be obtained in the capillary in a single experiment with higher efficiency, which will save lots of labor and time.

After the capillary was filled with the pre-mixed solution, FRET was used to monitor the stationary assembly behavior of the solution at different temperatures in the spatially varying temperature gradient; the results are shown in Fig. 3B. The temperature in the central region of the capillary was higher than the denaturation temperature of DNA, leading to no assembly; the free staple strand number 1–1 emitted strong fluorescence upon laser excitation. Along the temperature gradient, the temperatures on the two sides gradually decreased to the melting temperature of DNA; in this region, the origami assembly gradually began, thus resulting in a gradual decrease in the fluorescence intensity. The temperature gradient continually decreased along the two sides of the capillary, and the temperature was evidently lower than the melting temperature of DNA. Because the origami could not assemble effectively, the fluorescence intensity gradually recovered to the maximum. Lane 11 in Fig. 2F is the gel electrophoresis result of the solution collected from the capillary. Because only part of the solution was in the temperature region suitable for assembly, only a blurred origami band was observed in the electrophoresis result. With this method, the temperature corresponding to the maximal origami assembly efficiency can be obtained. As a result, this method can provide some guidance in identifying the ideal assembly temperature for the isothermal assembly of origami with different structures.

Additionally, the denaturation behavior of the assembled origami in the capillary in the spatially varying temperature gradient can be monitored; the fluorescence distribution along the capillary is shown in Fig. 3C. The temperature at the central region of the capillary is higher than the denaturation temperature, resulting in the dissociation of origami and thus the emission of strong fluorescence. For the regions at the two sides, the temperature gradually decreased to below the melting temperature; thus, the origami remained in an intact state and did not emit strong fluorescence. The transition region can be considered as the denaturation curve of the origami which was very similar

to the denaturation curve of nucleic acids. The capillary was then rapidly placed inside ice water, and the solution in the capillary was collected for gel electrophoresis separation; the result is shown in lane 10 in Fig. 2F. Only part of the origami was degraded. Therefore, more marked origami bands appeared. From this temperature gradient, the stability of origami at different temperatures can be determined. In addition, the average dissociation temperature of origami can also be obtained.

4. Conclusions

In this paper, a spatially varying temperature field was used to transform the temporal gradient in temperature to spatial temperature gradient along the microchannel. And then the dynamic process caused by the temperature or its change was set as a stable distribution of this process in space, where the time of process was frozen along the microchannel. This “time-frozen” technique has two major advantages. First of all, it saves labor and time by obtaining all thermodynamic characteristics under all different temperatures in a single test. Second, it provides enough time to investigate the rapid thermodynamic process of origami by transfer such time-varying process into a spatial-varying process along the microchannel, thus, the rapid thermodynamic process can be easily studied without the need of sophisticated and expensive instruments. By extending this method, kinetic or thermodynamic parameters, such as the diffusion coefficient, may be obtained. This method was demonstrated in two kinds of applications where the solution inside the microchannel was kept in flowing or stationary state. Those applications included the origami's assembly, strand displacement and localized investigation of origami's assembly and denaturation behaviors. This “time-frozen” technique is a very convenient method to evaluate the rapid response processes that occur for origami during a temperature change and can promote such research to certain extents.

Acknowledgements

This research was supported by the National Natural Science Foundation of China (No. U1505243), the Key Project of College Youth Natural Fund of Fujian Province (No. JZ160404), the guiding project of Fujian Province of China (No. 2016H0036), the funding from Xiamen Southern Oceanographic Center (Grant 14GHS016NF16) and the funding from Qinghai Province of China (2017-ZJ-750). Thank to Yange Wang for his help in AFM scanning.

Declarations of interest

None.

Credit author statement

H. C. and H. P. supervised the research. H. C. and H. P. conceived the research, designed the experiments. P. H. and J. W. carried out experiments and characterization. L. J. carried out the simulation. D. G. carried out the gel electrophoresis. S. J., M. L. and W. L. setup the temperature gradient and detection system. P. H., H. C. and H. P. interpreted data and wrote the paper.

Appendix A. Supplementary material

Supplementary data associated with this article can be found in the online version at https://doi.org/10.1016/j.bios.2019.02.012.

References

Andersen, E.S., Dong, M., Nielsen, M.M., Jahn, K., Subramani, R., Mamdouh, W., Golas, M.M., Sander, B., Stark, H., Oliveira, C.L.P., Pedersen, J.S., Birkedal, V., Besenbacher, F., Gothelf, K.V., Kjems, J., 2009. Nature 459, 73–76.
Cai, L.F., Zhu, Y., Du, G.S., Fang, Q., 2012. Anal. Chem. 84, 446–452.
Castro, C.E., Kilchherr, F., Kim, D.N., Shiao, E.L., Wauer, T., Wortmann, P., Bathe, M., Dietz, H., 2011. Nat. Methods 8, 221–229.
Chen, L., Chao, J., Qu, X., Zhang, H., Zhu, D., Su, S., Aldalbahi, A., Wang, L., Pei, H., 2017. ACS Appl. Mater. Interfaces 9, 8014–8020.
Chiu, D.T., Jeon, N.L., Huang, S., Kane, R.S., Wargo, C.J., Choi, I.S., Ingber, D.E., Whitesides, G.M., 2009. Proceedings Natl. Acad. Sci. 97, 2408–2413.
Clausell-Tormos, J., Lieber, D., Baret, J.C., El-Harrak, A., Miller, O.J., Frenz, L., Blouwolff, J., Humphry, K.J., Koster, S., Duan, H., Holtze, C., Weitz, D.A., Griffiths, A.D., Merten, C.A., 2008. Chem. Biol. 15, 427–437.
Derr, N.D., Goodman, B.S., Jungmann, R., Leschziner, A.E., Shih, W.M., Reck-Peterson, S.L., 2012. Science 338, 662–665.
Dietz, H., Douglas, S.M., Shih, W.M., 2009. Science 325, 725–730.
Ding, B., Deng, Z., Yan, H., Cabrini, S., Zuckermann, R.N., Bokor, J., 2010. J. Am. Chem. Soc. 132, 3248–3249.
Douglas, S.M., Dietz, H., Liedl, T., Hogberg, B., Graf, F., Shih, W.M., 2009a. Nature 459, 414–418.
Douglas, S.M., Marblestone, A.H., Teerapittayanon, S., Vazquez, A., Church, G.M., Shih, W.M., 2009b. Nucleic Acids Res. 37, 5001–5006.
Du, W.B., Fang, Q., Fang, Z.L., 2006. Anal. Chem. 78, 6404–6410.
Dunn, K.E., Dannenberg, F., Ouldridge, T.E., Kwiatkowska, M., Turberfield, A.J., Bath, J., 2015. Nature 525, 82–86.
Fu, Y., Zeng, D., Chao, J., Jin, Y., Zhang, Z., Liu, H., Li, D., Ma, H., Huang, Q., Gothelf, K.V., Fan, C., 2013. J. Am. Chem. Soc. 135, 696–702.
Garcia, E., Hasenbank, M.S., Finlayson, B., Yager, P., 2007. Lab Chip 7, 249–255.
Gu, S.Q., Zhang, Y.X., Zhu, Y., Du, W.B., Yao, B., Fang, Q., 2011. Anal. Chem. 83, 7570–7576.
Han, D., Pal, S., Nangreave, J., Deng, Z., Liu, Y., Yan, H., 2011. Science 332, 342–346.
Jiang, Q., Song, C., Nangreave, J., Liu, X., Lin, L., Qiu, D., Wang, Z.G., Zou, G., Liang, X., Yan, H., Ding, B., 2012. J. Am. Chem. Soc. 134, 13396–13403.
Jin, D.Q., Zhu, Y., Fang, Q., 2014. Anal. Chem. 86, 10796–10803.
Kakuta, M., Hinsmann, P., Manz, A., Lendl, B., 2003. Lab Chip 3, 82–85.
Kühler, P., Roller, E.M., Schreiber, R., Liedl, T., Lohmuller, T., Feldmann, J., 2014. Nano Lett. 14, 2914–2919.
Lai, W., Ren, L., Tang, Q., Qu, X., Li, J., Wang, L., Li, L., Fan, C., Pei, H., 2018. ACS Nano 12, 7093–7099.
Lee, C.C., Sui, G., Elizarov, A., Shu, C.J., Shin, Y.S., Dooley, A.N., Huang, J., Daridon, A., Wyatt, P., Stout, D., Kolb, H.C., Witte, O.N., Satyamurthy, N., Heath, J.R., Phelps, M.E., Quake, S.R., Tseng, H.R., 2005. Science 310, 1793–1796.
Liu, W., Zhong, H., Wang, R., Seeman, N.C., 2011. Angew. Chem. 123, 278–281.
Nangreave, J., Han, D., Liu, Y., Yan, H., 2010. Curr. Opin. Chem. Bilo. 14, 608–615.
Pinheiro, A.V., Han, D., Shih, W.M., Yan, H., 2011. Nat. Nanotech. 6, 763–772.
Qi, L., Xiao, M., Wang, X., Wang, C., Wang, L., Song, S., Qu, X., Li, L., Shi, J., Pei, H., 2017a. Anal. Chem. 89, 9850–9856.
Qi, L., Xiao, M., Wang, F., Wang, L., Ji, W., Man, T., Aldalbahi, A., Khan, M.N., Periyasami, G., Rahaman, M., Alrohaili, A., Qu, X., Pei, H., Wang, C., Li, L., 2017b. Nanoscale 9, 14184–14191.
Qu, X., Wang, Y., Shi, Z., Fu, G., Zeng, X., Li, X., Chen, H., 2012. Biosens. Bioelectron. 38, 342–347.
Qu, X., Zhu, D., Yao, G., Su, S., Chao, J., Liu, H., Zuo, X., Wang, L., Shi, J., Wang, L., Huang, W., Pei, H., Fan, C., 2017a. Angew. Chem. Int. Ed. 56, 1855–1858.
Qu, X., Wang, S., Ge, Z., Wang, J., Yao, G., Li, J., Zuo, X., Shi, J., Song, S., Wang, L., Li, L., Pei, H., Fan, C., 2017b. J. Am. Chem. Soc. 139, 10176–10179.
Qu, X., Li, M., Zhang, H., Lin, C., Wang, F., Xiao, M., Zhou, Y., Shi, Y., Aldalbahi, A., Pei, H., Chen, H., Li, L., 2017c. ACS Appl. Mater. Interfaces 9, 31568–31575.
Qu, X., Yang, F., Chen, H., Li, J., Zhang, H., Zhang, G., Li, L., Wang, L., Song, S., Tian, Y., Pei, H., 2017d. ACS Appl. Mater. Interfaces 9, 16026–16034.
Qu, X., Zhang, H., Chen, H., Aldalbahi, A., Li, L., Tian, Y., Weitz, D.A., Pei, H., 2017e. Anal. Chem. 89, 3468–3473.
Rothemund, P.W.K., 2006. Nature 440, 297–302.
Sacca, B., Niemeyer, C.M., 2012. Angew. Chem. Int. Ed. 51, 58–66.
Sato, K., Hibara, A., Tokeshi, M., Hisamoto, H., Kitamori, T., 2003. Adv. Drug Deliv. Rev. 55, 379–391.
Seeman, N.C., 2007. Mol. Biotechnol. 37, 246–257.
Shi, W., Qin, J., Ye, N., Lin, B., 2008. Lab Chip 8, 1432–1435.
Song, J., Arbona, J.M., Zhang, Z., Liu, L., Xie, E., Elezgaray, J., Aime, J.P., Gothelf, K.V., Besenbacher, F., Dong, M., 2012. J. Am. Chem. Soc. 134, 9844–9847.
Song, J., Zhang, Z., Zhang, S., Liu, L., Li, Q., Xie, E., Gothelf, K.V., Besenbacher, F., Dong, M., 2013. Small 9, 2954–2959.
Torring, T., Voigt, N.V., Nangreave, J., Yan, H., Gothelf, K.V., 2011. Chem. Soc. Rev. 40, 5636–5646.
Wah, J.L.T., David, C., Rudiuk, S., Baigl, D., Estevez-Torres, A., 2016. Acs Nano 10, 1978–1987.
Wei, X., Nangreave, J., Jiang, S., Yan, H., Liu, Y., 2013. J. Am. Chem. Soc. 135, 6165–6176.
Wei, X., Nangreave, J., Liu, Y., 2014. Acc. Chem. Res. 47, 1861–1870.
Whitesides, G.M., 2006. Nature 442, 368–373.
Yager, P., Edwards, T., Fu, E., Helton, K., Nelson, K., Tam, M.R., Weigl, B.H., 2006. Nature 442, 412–418.
Yao, G., Pei, H., Li, J., Zhao, Y., Zhu, D., Zhang, Y., Lin, Y., Huang, Q., Fan, C., 2015. NPG Asia Mater. 7, e159.
Zhong, R., Tang, Q., Wang, S., Zhang, H., Zhang, F., Xiao, M., Man, T., Qu, X., Li, L., Zhang, W., Pei, H., 2018. Adv. Mater. 30, 1706887.